

The detection of an extraordinarily-luminous high-redshift optical/ultraviolet flare by *Swift*/UVOT

Zhi-Ping Jin^{1,2,3†}, Hao Zhou^{1,2,3†}, Yun Wang^{1,3}, Jin-Jun Geng¹,
 Stefano Covino⁴, Xue-Feng Wu^{1,3}, Xiang Li¹,
 Yi-Zhong Fan^{1,2,3*}, Da-Ming Wei^{1,2,3}, and Jian-Yan Wei⁵

¹Purple Mountain Observatory, Chinese Academy of Sciences, Nanjing 210023, China

²Key Laboratory of Dark Matter and Space Astronomy of Chinese Academy of Sciences,
 Nanjing 210023, China

³School of Astronomy and Space Science, University of Science and Technology of China,
 Hefei 230026, China

⁴INAF/Brera Astronomical Observatory, via Bianchi 46, I-23807 Merate (LC), Italy

⁵National Astronomical Observatories, Chinese Academy of Sciences, Beijing 100049, China

*To whom correspondence should be addressed; E-mail: yzfan@pmo.ac.cn.

†These authors contributed equally to this work.

Hyper-luminous optical/ultraviolet flares have been detected in Gamma-ray Bursts and the record was held by naked eye event GRB 080319B. Such flares are widely attributed to internal shock or external reverse shock radiation. With a new dedicated method developed to derive reliable photometry from saturated images of *Swift*/UVOT, here we carry out time-resolved analysis of the initial White band 150 s exposure of GRB 220101A, a burst at the redshift of 4.618, and report a rapidly-evolving optical/ultraviolet flare with an unprecedented-high absolute AB magnitude ~ -39.4 . At variance with GRB 080319B, the temporal behavior of this new flare does not trace the gamma-ray activities. Rather than either internal shocks or reverse shock, this opti-

cal/ultraviolet monster is most likely from the refreshed shocks induced by the catching-up of the late-ejected extremely-energetic material with the earlier-launched decelerating outflow. We detect the first ultraviolet/optical flare with an absolute AB magnitude brighter than -39 and reveal the efficient process to power such transients.

Gamma-ray bursts are widely believed to originate from the internal energy dissipation of a highly relativistic and narrowly collimated outflow that was launched by a nascent stellar mass black hole or magnetized neutron star. Shortly after the onset of prompt emission of GRBs, there could come very bright optical/ultraviolet flashes arising from either the internal shocks in specific conditions or the external reverse shock radiation (1). An apparent ~ 9 th mag optical radiation was detected in GRB 990123 at a redshift of $z = 1.62$ (2, 3). Its rapid rise and the quick decline are consistent with the reverse shock radiation model (4–6), and the late more-detailed afterglow modeling revealed that the reverse shock region should be significantly more magnetized than the forward shock region (7, 8). A long-holding record was set by GRB 080319B, a burst at a redshift of $z = 0.937$. Its peak visual magnitude reaches 5.3 (corresponding to an absolute AB magnitude of -38.7), which is so bright that an observer in a dark location could have seen it with the naked eyes (9)! The correlated temporal behaviors of the prompt gamma-ray emission and the optical radiation are in favor of the internal shock process (10, 11). In the past decade, no similar or even comparable events have been reported.

GRB 220101A was discovered simultaneously by *Swift* Burst Alert Telescope (BAT) (12), the Fermi satellite (13) and the AGILE satellite (14). Before the so-called finding chart exposure ranging from 90 to 240 seconds with the White filter (12), UVOT observed the target in V band for 9 seconds. The estimated average magnitude in the White band for an exposure of ~ 150 s is ~ 14.7 th Vega mag (12, 15). The redshift was measured to be $z = 4.618$ and in the spectrum a broad absorption feature, which results from the Lyman alpha absorption (16, 17), is evident

centered at $\sim 6820 \text{ \AA}$. The corresponding isotropic equivalent gamma-ray energy is $\sim 4 \times 10^{54} \text{ erg}$ and the peak luminosity is $\sim 9 \times 10^{53} \text{ erg s}^{-1}$, both are in the rank of the brightest ones among current GRBs (18, 19). After the redshift correction, the observed optical photons were intrinsically in the ultraviolet bands. Therefore, all the emission detected by *Swift* suffered from serious absorption (in the observer's frame, the V band absorption is about 2 mag stronger than that in the I-band (16)) and thus the intrinsic emission would be much brighter. This is in particular the case for the White filter because of its large effective area in the blue part (i.e., U, UVW1, UVM2 and UVW2) and the Lyman alpha/intergalactic medium (IGM) absorption would be very strong. We concentrate on the first $\sim 150 \text{ s}$ exposure with White filter in the event mode (i.e. photon counting mode) that can be efficiently divided into short bins according to the signal-to-noise ratio (SNR). Our time-resolved analysis reveals that the measurements in the time range of $\sim 106 - 150 \text{ s}$ after the BAT trigger suffered from *strong saturation*, as shown in Fig. 1, Table S5 and Fig. S1. The absence of clear signal of the read-out streaks in the raw data, indicating a moderate saturation, however hampers a correction following procedures proposed in the literature (20, 21). Therefore we propose a new method to correct the saturation effect. The basic idea is that though the pile up at the source site is so serious that can not be reliably corrected, the surrounding but relatively “separated” pixels are possibly unaffected by saturation and therefore the enhancement of the counts should be correlated with the intrinsic count rate of the source. To clarify whether it is the case, we need some data with known magnitudes as well as the count rates in external annuli. For the unsaturated data with relatively low ring count rate, we simply take UVOT/White measurements of GRB 220101A at 150 – 240 seconds after the burst trigger. For the moderate saturation that is of our great interest, we take the UVOT measurements of GRB 130427A in the time interval of 500 – 2000 seconds. Though the moderately saturated White band emission of GRB 130427A can not be directly measured, we infer them with the UVOT emission in other bands since the spectrum can be

well fitted by a single power-law, see Fig. S2. With these two sets of data, we do find a tight correlation between photon count rate in $5''$ aperture (\dot{N}_{aper} , directly measured if unsaturated, or inferred from the “intrinsic” count rate \dot{N}_{int} measured in other ways) and in the $15'' - 25''$ ring (\dot{N}_{ring} , directly measured in UVOT images), which reads $\dot{N}_{\text{aper}} = (22.22 \pm 0.84)\dot{N}_{\text{ring}}$ for $\dot{N}_{\text{ring}} \leq 80 \text{ s}^{-1}$ (see Fig. S3). The correlation efficient for such an empirical relation is 0.99 (22). The other essential correction is on the absorption of the ultraviolet photons at high redshift. In the analysis we correct such a factor, i.e., 4.78 ± 0.10 mag in the White band, with the wide band energy spectrum and further check it with the other two GRBs at rather similar redshifts (see Fig. S5).

In Fig. 1 we show the lightcurves of the prompt gamma-ray emission and the very early optical emission. The first White exposure with a duration of 150 s was in the events mode. In our approach, a bin size of 4s is adopted. In principle, a narrower bin size is helpful in revealing the peak or structure of the flash, but a reasonably wide bin is necessary for a high SNR. The optical/ultraviolet flash lightcurve is relatively smooth and there is no evidence for tracing the temporal behavior of prompt gamma-rays. This is very different from the case of GRB 080319B, where the naked-eye optical flash shows strong variabilities and the optical lightcurve resembles that of the gamma-rays (see the insert of Fig. 1), indicating a new origin. We have also constructed the “prompt” optical, X-ray and gamma-ray SED. In Fig. 2 we show three representative time intervals of the first UVOT White band exposure, including the very beginning, the peak, and the final shallow decline phase. In the rise and the quick decline phases, the extrapolation of the high energy radiation spectrum into the optical is well below the White band measurements, which again points towards different physical origins of the optical and high energy radiation. While in the $t^{-2.3 \pm 0.3}$ shallow decline phase, the optical to X-ray emission are consistent with being a single power-law, which may be dominated by the external reverse shock radiation. In Fig. 3 we present the absolute AB magnitudes of the

very early optical emission of GRB 220101A and the other three remarkable events, including GRB 990123 (3), GRB 050904 (23) and GRB 080319B (9), distinguished by the extremely bright optical emission. After the proper saturation, absorption and cosmological corrections, it turns out that GRB 220101A sets a new record. The prompt ultraviolet to X-ray spectrum at the optical/ultraviolet emission peak time is softer than $\nu^{-1.3}$ (see Fig.2). If this soft spectrum could extend to the optical band in the frame of the burst, GRB 220101A would be so far the unique source with an absolute AB magnitude brighter than -40 in the visible band (22). Note that the peak optical emission of GRB 220101A could be even stronger than presented here since our current fluxes are the average of the radiation in each 4s bin.

As already mentioned before, for GRB 080319B, the internal shock model is favored by the similar temporal behaviors of the prompt gamma-ray and optical radiation. While for GRB 990123, the external reverse shock model has been widely accepted to account for the optical flash. The optical/ultraviolet flare detected in GRB 220101A, however, should have a different physical origin for the following facts: (i) In contrast to GRB 080319B, the optical flash lightcurve of GRB 220101A does not trace the variability of the prompt gamma-rays (see Fig. 1), requiring different radiation processes/sites of these two components; (ii) The $t^{-2.3}$ -like decline of the optical/ultraviolet flare of GRB 220101A may be due to the reverse shock emission, but the $\sim t^{20}$ increase is much quicker than that of GRB 990123 and hence strongly in tension with the standard external reverse/forward shock emission model (5, 6). Here we present a refreshed shock model for the brightest optical/ultraviolet spike of GRB 220101A. Looking at the gamma-ray lightcurve, the main burst phase consisting of two giant gamma-ray spikes appears at ~ 90 s after the BAT trigger, and the earlier emission was much weaker (i.e., the time-averaged luminosity is $\sim 10^{52}$ erg s $^{-1}$). As indicated by the bulk Lorentz factor–luminosity correlation (24, 25) of $\Gamma \propto L_{\gamma}^{0.3}$, the weak/slow GRB outflow component launched at the early times is expected to have a $\Gamma \sim 10^2$ and the surrounding interstellar medium further decelerates

the outflow to a Lorentz factor of Γ_W , while the outflow component yielding the most luminous part of GRB 220101A likely has a Lorentz factor of $\Gamma_M \sim 10^3$. The first giant spike comes from the energy release of the main outflow, either through the internal shocks or the magnetic re-connection within it. Soon the main outflow would catch up with the decelerating weak part at a time of $\sim \Gamma_W^2 \delta t_{WM} / \Gamma_M^2 \sim \mathcal{O}(10)$ s, which explains the second gamma-ray spike and the delayed onset of the optical/ultraviolet flare, where $\delta t_{WM} \sim 100$ s is the delay of the onset of the main part with respect to that of the weak part (started at ~ 60 s before the trigger, see Fig. 1). The collision of the late/fast material shell(s) with the early/decelerating material will generate strong refreshed shocks and then produce energetic emissions. Following the treatments presented in Sec. 2.1 of the Ref. (26), it is straightforward to show that for the internal shocks taking place at $\sim 2\Gamma_W^2 c \delta t_{WM} / (1+z) \sim 10^{16}$ cm $(\Gamma_W/10^2)^2 (\delta t_{WM}/10^2$ s), the typical synchrotron radiation frequency is indeed within the optical/ultraviolet bands. The bulk Lorentz factor of the merged shells can be approximated to be $\bar{\Gamma} \approx \sqrt{[M_W \Gamma_W + M_M \Gamma_M] / [M_W / \Gamma_W + M_M / \Gamma_M]}$ and the Lorentz factor of the internal shocks can be estimated as $\Gamma_{sh} \approx \Gamma_M / \bar{\Gamma} + \bar{\Gamma} / \Gamma_M$, where M_W and M_M are the rest masses of the ejecta powering earlier weak gamma-ray emission and the main outburst, respectively (27). Indeed, for GRB 220101A-like burst, we have the outflow luminosity of $L_m \sim 10^{53} - 10^{54}$ erg s $^{-1}$, with the fractions of the shock energy given to the magnetic fields (electrons) $\epsilon_B \sim 0.1$ ($\epsilon_e \sim 0.3$), $\bar{\Gamma} \sim \text{several} \times 100$ and $\Gamma_{sh} \sim \text{a few}$, it is natural to have an optical/ultraviolet flux (26) of ~ 1 Jy even for a redshift as high as ~ 5 (a numerical example is presented in (22) and Fig.S6).

Note that the very energetic prompt emission appearing at $\sim T_0 + 90$ s, which partly overlap with the optical/ultraviolet flash, after the BAT trigger should also effectively cool the electrons accelerated in the collision discussed above. Such a process would produce GeV emission, which is expected to last longer than the overlapping phase of the prompt MeV emission and ultraviolet/optical flare. Indeed, at $t \sim 100 - 150$ s after the BAT trigger, GeV emission was

detected from GRB 220101A (28).

Though the hyper-luminous very early optical/ultraviolet emission are not common, we suggest that the bursts with prompt emission resembling GRB 220101A (i.e., the much more energetic outflow is well separated from the early ejecta) are good candidates for hosting the extraordinarily bright flares. The problem is how to catch such signals promptly. Small telescopes with a large field of view should be very helpful and the I/R -band observation of these telescopes can catch the monsters in a wide range of redshifts. Anyhow, such observations are limited by the weather, the time (day or night) and the burst site. The space telescopes like *Swift*/UVOT and SVOM/VT (29) may play an important role for the high redshift events. Since the optical/ultraviolet flash of GRB 220101A was observed by *Swift*/UVOT, below we focus on the upcoming 0.4m SVOM/VT with two channels, including the blue (400 – 650 nm) and the red (650 – 1000 nm) bands. For the shortest exposure time of 1s, the saturation limit is about 9th magnitude. Given its higher sensitivity in comparison to *Swift*/UVOT V filter, the seriously absorbed “ultraviolet” emission of GRB 220101A/GRB 080319B-like extra-luminous events, even taking place at the even higher redshift (say, $z \sim 6$), can still be caught by the blue channel of SVOM/VT though the red channel might be saturated (22). Dedicated observation strategies are needed to optimize the potential of the discoveries.

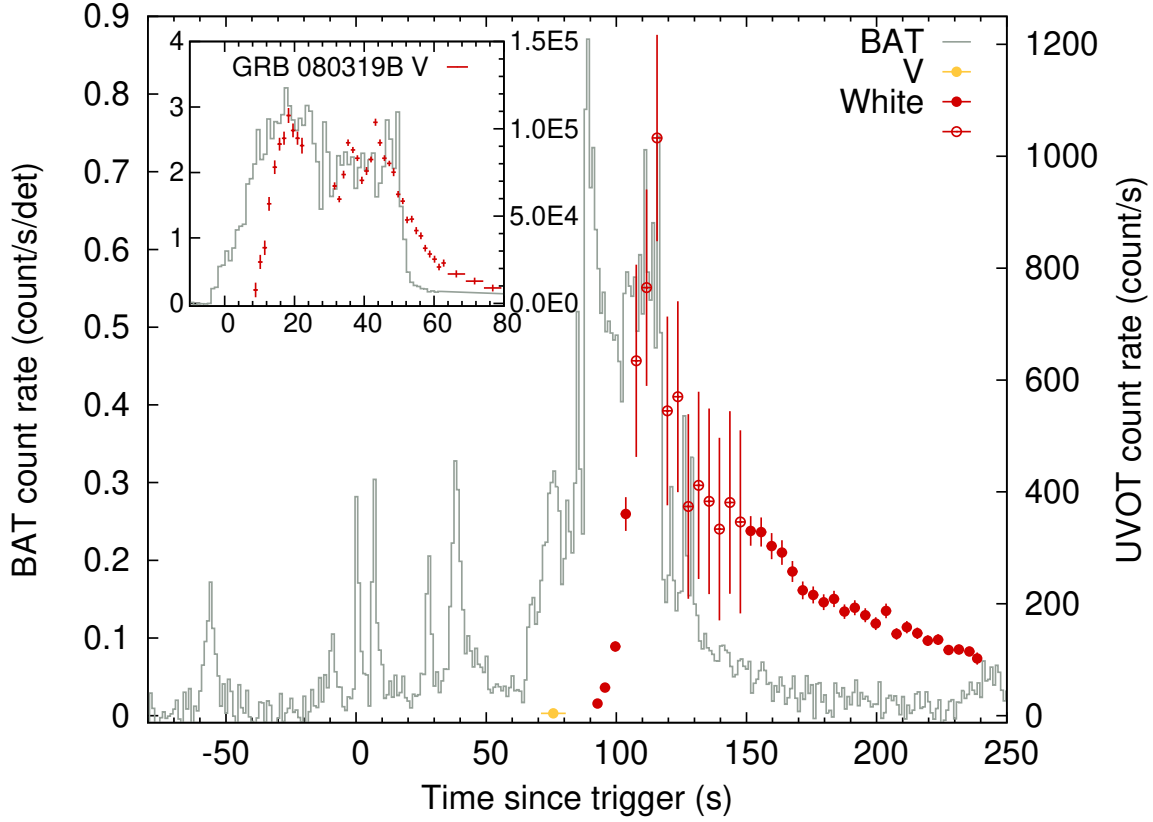


Figure 1: **Photon count rates of the prompt gamma-ray (Swift/BAT) and optical (Swift/UVOT V and White band) emission of GRB 220101A.** The prompt gamma-ray lightcurve is highly variable, while the prompt optical emission lightcurve is relatively smooth and does not trace that of gamma-rays. The red filled circles are from the aperture measurement while the open circles are obtained with the new method developed in this work. The energetic optical/ultraviolet flash just overlaps with the late part of the giant outburst phase of the prompt gamma-rays. The prompt gamma-ray and optical lightcurves of GRB 080319 are inserted for comparison.

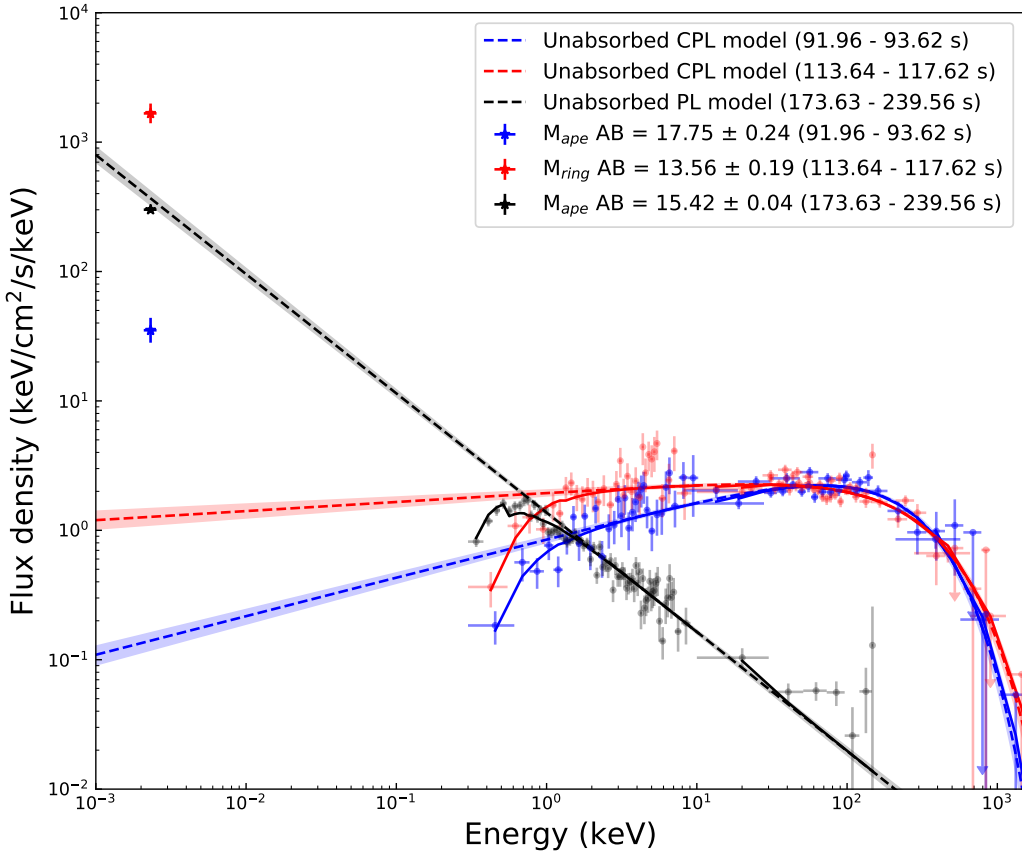


Figure 2: **The “prompt” optical to γ -ray SEDs of GRB 220101A.** The data in blue (red) are collected in the very beginning (peak) of the UVOT/White band emission. The optical emission in both cases are well above the extrapolation of the high energy spectrum, suggesting an origin different from the prompt X-rays and gamma-rays. While in the time interval of $t \sim 173.6 - 239.6$ seconds, the extrapolation of the X-ray and gamma-ray spectrum into the optical is in agreement with the UVOT data.

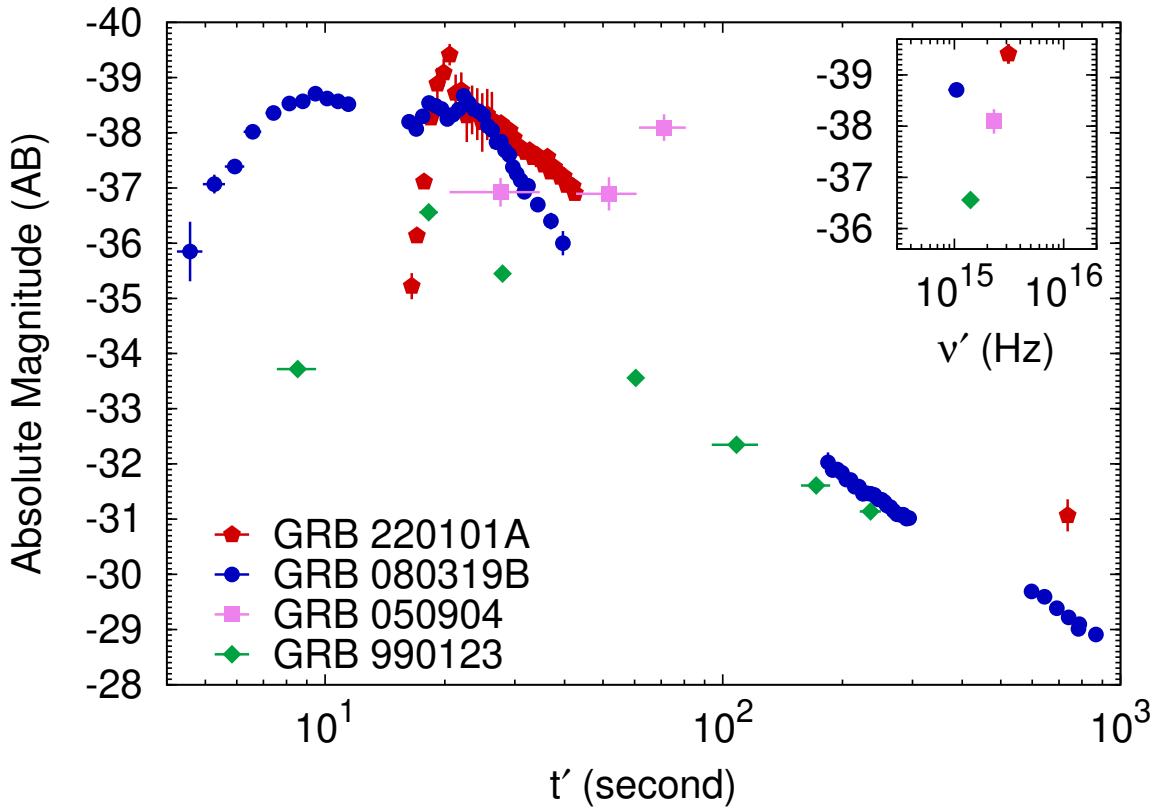


Figure 3: **The ultraviolet/optical flare of GRB 220101A (red) in comparison to that of GRB 990123 (green) (3), GRB 050904 (pink) (23) and GRB 080319B (blue) (9) in rest frame.** The White band emission of GRB 220101A has been corrected for total extinction of $A_\lambda = 4.78 \pm 0.1$ mag, including the tiny softening of $E(B - V) = 0.0483$ mag in the Milky Way. The absolute AB magnitude of GRB 220101A exceeds that of GRB 080319B, the so-called naked burst, rendering it the most energetic optical/ultraviolet flare recorded so far.

References

1. P. Mészáros, M. J. Rees, *Astrophys. J.* **476**, 232 (1997).
2. M. I. Andersen, *et al.*, *Science* **283**, 2075 (1999).
3. C. Akerlof, *et al.*, *Nature* **398**, 400 (1999).

4. A. J. Castro-Tirado, *et al.*, *Science* **283**, 2069 (1999).
5. R. Sari, T. Piran, *Astrophys. J.* **520**, 641 (1999).
6. P. Mészáros, M. J. Rees, *Mon. Not. Roy. Astron. Soc.* **306**, L39 (1999).
7. Y.-Z. Fan, Z.-G. Dai, Y.-F. Huang, T. Lu, *Chin. J. Astron. Astrophys.* **2**, 449 (2002).
8. B. Zhang, S. Kobayashi, P. Mészáros, *Astrophys. J.* **595**, 950 (2003).
9. J. L. Racusin, *et al.*, *Nature* **455**, 183 (2008).
10. Y.-Z. Fan, B. Zhang, D.-M. Wei, *Phys. Rev. D* **79**, 021301 (2009).
11. Z. Li, E. Waxman, *Astrophys. J. Lett.* **674**, L65 (2008).
12. A. Tohuvavohu, *et al.*, *GRB Coordinates Network* **31347**, 1 (2022).
13. S. Lesage, C. Meegan, Fermi Gamma-ray Burst Monitor Team, *GRB Coordinates Network* **31360**, 1 (2022).
14. A. Ursi, *et al.*, *GRB Coordinates Network* **31354**, 1 (2022).
15. N. P. M. Kuin, A. Tohuvavohu, Swift/UVOT Team, *GRB Coordinates Network* **31351**, 1 (2022).
16. S. Y. Fu, Z. P. Zhu, D. Xu, X. Liu, S. Q. Jiang, *GRB Coordinates Network* **31353**, 1 (2022).
17. J. P. U. Fynbo, *et al.*, *GRB Coordinates Network* **31359**, 1 (2022).
18. J. L. Atteia, *GRB Coordinates Network* **31365**, 1 (2022).
19. A. Tsvetkova, *et al.*, *GRB Coordinates Network* **31433**, 1 (2022).
20. M. J. Page, *et al.*, *Mon. Not. Roy. Astron. Soc.* **436**, 1684 (2013).

21. P. W. A. Roming, *et al.*, *Astrophys. J. Supp.* **228**, 13 (2017).
22. Materials and methods are available as supplementary materials.
23. M. Bo  r, *et al.*, *Astrophys. J. Lett.* **638**, L71 (2006).
24. J. L  , *et al.*, *Astrophys. J.* **751**, 49 (2012).
25. Y.-Z. Fan, D.-M. Wei, F.-W. Zhang, B.-B. Zhang, *Astrophys. J. Lett.* **755**, L6 (2012).
26. D. M. Wei, T. Yan, Y. Z. Fan, *Astrophys. J. Lett.* **636**, L69 (2006).
27. T. Piran, *Phys. Rept.* **314**, 575 (1999).
28. M. Arimoto, L. Scotton, F. Longo, Fermi-LAT Collaboration, *GRB Coordinates Network* **31350**, 1 (2022).
29. S.-J. Yu, F. Gonzalez, J.-Y. Wei, S.-N. Zhang, B. Cordier, *Chin. Astron. Astrophys.* **44**, 269 (2020).

Acknowledgments

Funding: This work was supported in part by NSFC under grants of No. 12225305, 11921003 and 11933010, the China Manned Space Project (NO.CMS-CSST-2021-A13), Major Science and Technology Project of Qinghai Province (2019-ZJ-A10), Key Research Program of Frontier Sciences (No. QYZDJ-SSW-SYS024). SC has been supported by ASI grant I/004/11/0.

Author Contributions: Y.Z.F and Z.P.J launched the project. Z.P.J, H.Z., Y.W, X.L, S.C and J.Y.W carried out the data analysis. Y.Z.F, J.J.G., X.F.W, D.M.W and Z.P.J interpreted the data. Z.P.J, H.Z. and Y.Z.F prepared the paper and all authors joined the discussion. Z.P.J and H.Z contributed equally.

Competing Interests: The authors declare that they have no competing financial interests.

Author Information: Correspondence and requests for materials should be addressed to Y.Z.F (yzfan@pmo.ac.cn).

Code availability: The codes used in this analysis are standard in the community, as introduced in the supplementary materials.

Data availability: The *Swift* observation data analysed/used in this work are all publicly available.

Supplementary materials

Materials and Methods

Tables S1 to S6

Figs. S1 to S7

References (30-52)

Materials and Methods

1 A new method to measure the saturated sources in *Swift* UVOT images

UVOT is a photon counting detector and typical read-out rate is once every ~ 11 ms. If the source is bright enough (> 10 counts s^{-1}), coincidence losses start to be significant and a correction is necessary. When the incident photon counts rate beyond the read-out rate ~ 86 s^{-1} , the source is fully saturated and proper coincidence loss correction is impractical (30). However for extremely saturated sources with read-out streaks, a calibration method has been developed based on the measurement of read-out streak line strength (20). Anyhow, the read-out streak lines are only present in the extremely saturated sources or those with very long time exposure. For the moderate saturation with relatively short exposure, it cannot be applied and our main goal is to provide a new way. Below we focus on the White band, but our method can be applied to other UVOT filters as well (indeed, as a validation, we also show in the end of this subsection that a rather similar empirical correction function holds for the V band).

The saturated pattern of an UVOT image can be divided into three parts. The first is a point source like structure at the center of saturated pattern, which represents the location of the saturated source. The second part is a dark square structure caused by coincidence loss and the half length of its diagonal line is about 14 arcsec. A more detailed explanation is that UVOT has

actually a 256×256 CCD which records the flash pattern produced by the incident photon after several amplifiers and there is a centroid algorithm to calculate positions of incident photons whose accuracy could reach 0.125 pixel. As a result, each physical pixel could be subsampled to 8×8 virtual pixels with a resolution of 0.5 arcsec/pixel. The side length of the dark square is about 20 arcsec, that is 40 virtual pixels, corresponding to an area of 5×5 pixels region on real physical CCD which is the affected region of coincidence loss. The third part is the halo ring, which is distinct for saturated sources and some unsaturated sources but with low background. Fig. S1 shows such a saturated pattern. We attribute the halo rings to the wing of the Point Spread Function (PSF) of UVOT detector. To test this conjecture, we will examine whether the “intrinsic” photon counts rates of saturated sources is proportional to photon counts rates of halo rings.

To avoid the influence of the coincidence loss, the best measurement region to get the highest S/N ratio is the area between a circle with a radius of 25 arcsec and a square, with the same center and with a side length of 20 arcsec, like a Chinese copper cash. However, if *Swift* rotated during observations, the dark region of final stacked science image are not necessarily a square due to that the coincidence loss square is aligned to the edge of CCD. Hence, we used an annulus of an inner radius of 15 arcsec and an outer radius of 25 arcsec (i.e., the outer edge of halo rings) to measure photon count rate in the ring (\dot{N}_{ring}), where the background should be removed and the coincidence loss has been corrected. The crucial step is to reliably derive the corresponding photon count rate of the saturated source within the standard aperture with a radius of 5 arcsec (\dot{N}_{aper}). As mentioned above, if the incident photon counts rate is beyond the CCD readout rate, the source is saturated. Fortunately, the UVOT White band is much wider than other 6 bands (hence, we will call them the narrow bands), which means although a source is saturated in White band, it could be unsaturated in narrow bands. It is therefore plausible to measure the spectrum with other filters of UVOT and then convolve it with the

White filter to get the corresponding “intrinsic” emission. This can be done for the power-law like afterglow spectrum of GRBs and the very early time optical flash of GRB 130427A is a nice sample. The earliest UVOT measurements of this burst were highly saturated and some of them can be analyzed with the readout streak method (20). Moreover, as shown in Maselli et al. (31) and the left panel of Fig. S2, when the White filter was still saturated, there were usable measurements in other bands. In the right panel of Fig. S2, we show the ultraviolet/optical SED of GRB 130427A with the UVOT observations. Note that these data were re-measured in this work and they are consistent with that reported in the literature (31). We performed the early time photometry of GRB 130424A with *HEASoft* and the results are summarized in Table S1. The first exposure in B band and the first 2 exposures in U band were saturated, hence we took the values from Maselli et al (31). Light curves of 6 narrow bands were fitted to found their magnitudes simultaneous with White band exposures, the results are listed in Table S2. We then carry out the power-law spectral fit to the SED and estimate the White band magnitudes, as summarized in the last column of Table S2, which are further used in Table S3 to yield the \dot{N}_{int} (in another word, the inferred \dot{N}_{aper}). It is worth noting that in epoch 1 there was an optical/ultraviolet flare and hence it is not suitable to evaluate the White band emission with this method. Moreover, the White band measurement in the first, second and third epochs were significantly saturated with readout streaks, for which the fluxes were reported before. As show in Fig. S3, in epoch 2 our calculated flux is consistent with that reported in Maselli et al. (31), validating the method proposed in this work. Our downloaded image of the epoch 3 mentioned in Maselli et al. (31) is distorted and we have hence focused on the subsequent observation data with an exposure of 20 s. Our estimated flux is still well consistent with that reported in Maselli et al. (31), which is expected because these two measurements were almost simultaneous. Anyhow, in the plot the data point reported in Maselli et al. (31) is not shown because we can not measure its ring count rate because of distortion. For epoch 4 to epoch

8, there were no readout streaks and the method developed by Page et al. (20) does not work any longer. Our method mentioned above applies to these data and yield reasonable results. As for GRB 220101A, shortly after its peak, the ultraviolet/optical flash is not saturated any more. For these observations we can reasonably measure its White band emission. *HEASoft* UVOT pipeline was used to make photometry of barely saturated images of GRB 220101A with a circle aperture with a radius of 5 arcsec. However, a reliable measurement of the ring count rate requires a somewhat long exposure. Therefore, we just divide the “tail” part of the flash into two time intervals. We also notice 3 bright stars in the field and then measure them for independent check. These five data points are summarized in Table S3. The White band fluxes measured (indirectly and directly, respectively) in the above events and field stars are used to clarify whether there is a tight correlation between the ring counts and the intrinsic source emission. For such a purpose, these three data sets have been fitted with a linear function of a model of $y = ax$ and a least square cost function was applied, $\chi^2 = \sum_i \frac{(y_i - ax_i)^2}{y_{\text{err},i}^2 + (ax_{\text{err},i})^2}$, where y_i and x_i represent extracted White-band photon counts rates and halo ring photon counts rates, respectively, and $y_{\text{err},i}$ and $x_{\text{err},i}$ are the corresponding uncertainties. The Pearson correlation coefficient is 0.99, which reveals a very strong linear correlation, and the $\chi^2/\text{d.o.f}$ value is ~ 0.90 , which implies a reasonable fit, where d.o.f denotes the degree of the freedom. Hence, we conclude that $\dot{N}_{\text{aper}} = 22.22 \pm 0.84 \dot{N}_{\text{ring}}$ can yield a reasonable estimation of “true” photon counts rates of saturated sources in White band. Fig. S3 presents our best fitting result which confirms our early speculation and suggests that the outer part of the PSFs of such sources are nearly unmodified.

The ground-based telescopes can well measure the V-band emission of the sources, which can thus provide an economical way to calibrate the saturated V-band observations of *Swift*/UVOT. Interestingly, GRB 080319B is a nice example. For the UVOT V-band observations, in total we have 22 sub event files, which were later converted to images with *HEASoft* for measurements.

The first 4 exposure duration are 30s, 40s, 50s and 55s, which are same as the time bins in Page et al. (20). These exposures display readout streaks and have been analyzed with the method of Page et al. (20), which are shown in the right panel of Fig. S3 (see the light green empty squares). We measured the counts rate in the halo rings, which is defined above, with *HEASoft*, but made coincidence loss correction manually. Another 18 images are unsaturated, the intrinsic emission were directly measured, and they are marked with dark green empty triangles in the right panel of Fig. S3. These measurements are summarized in Table S4. In addition, the optical emission of GRB 080319B was well measured by the ground based telescopes (32), and the accurately measured V-band emission from RAPTOR-T can be taken as the intrinsic ones (i.e., we have the \dot{N}_{int} , in another word, \dot{N}_{aper} defined in this paper). The difference between the V filter of UVOT and that of RAPTOR-T is small and the magnitude difference can be ignored, as demonstrated by the overlapping data points in the left lower corner of the right panel of Fig. S3. Since the very early UVOT/V band observations were in event mode, we can re-bin them into the time intervals the same as that of RAPTOR-T and then get the \dot{N}_{ring} . Time bins of our measurements are listed in Table S4. Therefore, we apply the linear fit to the data sets and find an empirical function of $\dot{N}_{\text{aper}} = 20.6 \pm 0.4 \dot{N}_{\text{ring}}$ with a high correlation coefficient of 0.998. Such a correlation is nicely consistent with that for the UVOT/White band. It is worth noting that for GRB 220101A, the photons collected in the White band are dominated by those passing the V filter because of the serious absorption in the bluer region. Indeed we find rather similar count rates for the (almost) simultaneous White and V-band measurements (see Fig. S4). Therefore, the rather similar correction function for UVOT/V filter strongly suggests that our White band analysis of GRB 220101A is robust.

2 Data analysis

2.1 *Swift* UVOT data analysis

Swift/UVOT observed GRB 220101A in V, B, U, W1, M2, W2 and White bands for several epochs. For data in image mode, we started from the level 2 UVOT products and used standard aperture photometry, background was measured in a nearby region without sources in stacked images. Reliable detections were only obtained in V and White bands, and the photon count rates were measured in 3 or 5 arcsec apertures, depending on SNR. Coincidences loss correction and aperture correction were applied. For images without detection, upper limits were assuming count rates would have reached the SNR of $S/N = 3$. Finally zeropoints including long-term sensitivity correction were used for absolute calibrations. The results are shown in Table S5.

The first white-band exposure under event mode (incident positions and time of every photon are recorded) began at about 90 seconds after the trigger time, which lasted about 150 seconds. Due to the fact that the luminosity of GRB 220101A changed rapidly at early epochs, although the transient seems to be unsaturated on the image for the total 150s exposure, it could be saturated in its peak phase. Hence, we screened the calibrated event data into slices whose exposure time is ~ 4 s to check whether the situation mentioned above had happened. Following the guidance of UVOT data process, event slices were transformed into images and image calibrations (flat field and mod 8 corrections) were applied. Since the transient is bright and isolated on reduced images, standard aperture photometry method was applied. From 90s to 100s, the transient was brightening rapidly and then became saturated for about 50 seconds. After ~ 150 s since the trigger time, it became unsaturated, again. We found that there are halo rings around the transient on barely saturated and saturated images, which we think are the 'wings' of point spread functions, hence, we analyzed the data with our calibration method described before. The results are summarized in Table S5.

2.2 *Swift*-BAT/XRT and Fermi-GBM data analysis

We processed *Swift*-BAT data according to standard procedures, using the software *HEASoft* (ver. 6.29) and calibration database (*CALDB*), which are available at

<https://www.swift.ac.uk/analysis/bat/setup.php>. The mask weighting file used in extracting the light curve is generated by *batgrbproduct* (a complete GRB processing script in *HEASoft*). We extract event data at time intervals between -60 to 340 seconds related to the trigger time, the energy range is 15-350 keV, and the time bin size is 1 second. Our BAT analysis results are plotted with our *Swift* UVOT analysis results in Fig. 1.

We also present a spectral analysis in a broad gamma-ray band (0.3 - 40000 keV) from *Swift*-BAT/XRT and Fermi-GBM data. The files used include the source and background spectrum files, as well as the corresponding response functions. For BAT file extraction and correction, we used standard procedures as in the manual (33). XRT files were created by online analysis tools provided by *Swift* official website (34, 35). The Fermi-GBM data have been processed with *GBM Data Tools* (36). There are different statistics used for each dataset (*cstat* for *Swift*-XRT, χ^2 for *Swift*-BAT and *pgstat* for Fermi-GBM data). We use *Bilby* (37) in the framework of *PyXspec* for model parameter estimation. The results are shown in Fig. 2.

3 Intrinsic optical/ultraviolet emission of GRB 220101A

To estimate a reliable un-absorbed optical/ultraviolet emission, we need an intrinsic spectrum to evaluate the absorption in different observation bands. For such a purpose, in addition to the UVOT V and White band observations, we adopt the g, r, i, z -band data from Liverpool telescope measured at $t \sim 0.625$ day after the burst (38) and the simultaneous XRT data. Such a set of ground-based telescope observation data are chosen because they are almost simultaneous with one UVOT White measurement and at late times the White band emission was not

detectable any longer (see Table S5 and Fig. S4). The SED from i to g declines very rapidly, requires a spectral index $\beta \sim 8$ (see Fig. S5). Similar rapid declines, due to the serious Lyman forest absorption, have been observed in GRB 000131 (39) and 100219A (40) at redshifts of $z = 4.500$ and 4.667 , respectively. Since the i and z observations do not suffer from strong absorption and there is no evidence for the presence of a flare at that time, we adopt them to construct the intrinsic optical (z band) to X-ray SED to be $f_\nu \propto \nu^{-0.70 \pm 0.05}$, with which we can obtain the absorption correction in r , g as well as UVOT White and V bands. In the direction of GRB 220101A, the Galactic extinction is $E(B - V) = 0.0483$ (41). Basing on the intrinsic spectrum of and assuming no extinction from the GRB host galaxy, we find an absorption in White band as high as $A_\lambda = 4.78 \pm 0.10$ mag, including Lyman absorption and the Galactic extinction, see the right panel of Fig. S5. Note that here the central frequency of the White band observation has been taken as the same as that of the V band because of the serious absorption of the bluer photons, as demonstrated in Fig. S4.

In this work we adopt a cosmology with $H_0 = 67.4 \text{ km s}^{-1} \text{ Mpc}^{-1}$, $\Omega_M = 0.315$ and $\Omega_\Lambda = 0.685$ (42), a redshift $z = 4.618$ leads to a distance modulus $\text{DM} = 48.19$. The absolute peak magnitude is calculated via $M_{\text{peak,abs}} = M_{\text{peak}} - \text{DM} - A_\lambda + 2.5(1 - \beta_i) \log(1 + z)$, where the last term is the k-correction and β_i is the intrinsic spectral slope. The pity is that none of the extremely luminous flashes in GRB 990123, GRB 050904, GRB 080319B and GRB 220101A have a measured optical/ultraviolet spectrum. For GRB 220101A, the UVOT and XRT data suggest an “overall” optical to soft X-ray spectrum softer than $\nu^{-1.3}$. If this holds in the optical band (i.e., $\beta_i \geq 1.3$) in the rest frame, then we would have $M_{\text{peak,abs}} \leq -40$ mag in the visible band. It is so far the unique event to be brighter than the absolute AB magnitude of -39 mag, see Table S6 for a comparison of the brightest flare in history. If there are spectral information of optical flares in the future, these bursts would be able to directly compared in the same band.

4 The numerical interpretation of the optical emission as well as the X-ray afterglow emission

Here we call the X-ray emission after ~ 170 s after the *Swift* trigger as the afterglow since the earlier emission are most likely the low energy part of the prompt radiation arising from the internal energy dissipation.

4.1 Refreshed shock emission for the peak of the optical/ultraviolet flare

In the prompt γ -ray emission lightcurve, there are several weak gamma-ray spikes from earlier outflow before the main pulse starting at $\sim T_0 + 65$ s. The front half part (between $\sim T_0 + 65$ to 102 s) of the giant gamma-ray pulse should come from the energy release of the main outflow, either dissipated through internal shocks or magnetic re-connections within it. For the later part ($> T_0 + 102$ s) of the giant pulse, it overlaps with an energetic optical/ultraviolet flash, which indicates the rise of an additional dissipation process. As the preceding weak outflow gets decelerated to a bulk Lorentz factor of Γ_1 , a later launched but faster shell (with a bulk Lorentz factor of Γ_4) will catch up with it at a radius of R_0 , so that a collision between two shells would occur. Note that Γ_1 and Γ_4 correspond to Γ_W and Γ_M mentioned in the main text, which is used here for the convenience of the discussion below. If the fast shell is not extremely magnetized, the collision would produce a refreshed forward shock (FS) propagating into materials of the preceding shell, and a refreshed reverse shock (RS) propagating into the fast shell. As a result, an optical/ultraviolet flash is expected from the radiation in the downstream of the refreshed RS, which has been initially proposed and works well for optical flash in the early afterglow stage (5). Here we show that this scenario could account for the prompt optical emission of GRB 220101A with a detailed numerical approach.

Two refreshed shocks separate the system into four regions: (1) the unshocked slow shell, (2) the shocked slow shell, (3) the shocked fast shell, and (4) the unshocked fast shell. Here-

after, X_i denotes the value of the quantity X in Region “ i ” in its own rest frame. Unlike the preceding shell that exhausts the magnetic energy in the early stage ($\sigma_1 = 0$), the later fast shell may keep the magnetic fields advected from the central engine, which could be parameterized by the magnetization of $\sigma_4 = B_4^2/4\pi n_4 m_p c^2$, where n_4 is the particle density in the comoving frame of Region 4 and m_p is the proton mass. Let’s introduce an equivalent “luminosity” of the kinetic, internal and the magnetic energy for the two shells measured in the lab frame, L_i , the corresponding particle density is then $n_i = L_i/4\pi R^2 \beta_i \Gamma_i^2 m_p c^3 (1 + \sigma_i)$, where $i = 1, 4$, $\beta_i = 1/\sqrt{1 - 1/\Gamma_i^2}$ and R is the radius from the central engine. Due to the highly variable nature of the outflow from the central engine, the luminosity of the later fast ejecta could be further described by $L_4 = L_f (R/R_{\text{peak}})^{q_r}$ for $R \leq R_{\text{peak}}$ and $L_4 = L_f (R/R_{\text{peak}})^{q_d}$ for $R > R_{\text{peak}}$, where R_{peak} is the radius that the RS reaches its peak luminosity, and q_r (q_d) is the rising (decaying) index of the luminosity before(after) R_{peak} . We assume that Region 2 and Region 3 share a common bulk Lorentz factor ($\Gamma_2 = \Gamma_3$). After applying the hydrodynamical/magnetohydrodynamical jump conditions (43, 44) to the FS/RS respectively and the energy conservation law to the FS-RS system (45), the evolution of Γ_2 and relevant quantities within these regions could be solved numerically given the total isotropic energy of each shell (E_f and E_s).

The kinetic particle-in-cell simulations reveal that particle acceleration is less efficient in strongly magnetized shock than that of weakly magnetized shock (46). The shock is considered to be moderately magnetized, and it is reasonable to assume that the distribution of electrons injected downstream is Maxwellian both for the FS/RS (47), i.e., $Q_i(\gamma_e, t) = C_i (\gamma_e/\gamma_{c,i})^2 \exp^{-\gamma_e/\gamma_{c,i}}$, where $\gamma_{c,i} = \frac{1}{3} \epsilon_{e,i} \frac{e_i}{\rho_i c^2} \frac{m_p}{m_e}$ is the typical Lorentz factor of the thermal distribution, $\epsilon_{e,i}$ is the fraction of post-shock energy that goes into electrons for each region, e_i and ρ_i is the energy and density of protons. The normalization constant C_i is obtained from the relevant mass conservation. The instantaneous electron spectrum can be obtained by solving the continuity equation of elec-

trons in energy space (48). Integrating the synchrotron radiation power from the electron spectrum in Regions 2 and 3 and considering the effect of synchrotron self-absorption and the equal-arrival-time surface, the radiation spectra and the light curves are then derived. With a starting radius of $R_0 = 10^{15}$ cm for the collision and a set of parameters of $L_1 = 5.6 \times 10^{52}$ erg s $^{-1}$, $L_f = 4.5 \times 10^{53}$ erg s $^{-1}$, $\Gamma_1 = 100$, $\Gamma_4 = 1000$, $q_r = 1.3$, $q_d = -0.5$, $\sigma_4 = 0.1$, $\epsilon_{B,3} = 0.08$, $\epsilon_{e,2} = 0.1$, $\epsilon_{e,3} = 0.07$, $E_s = 5.8 \times 10^{53}$ erg, $E_f = 6.0 \times 10^{54}$ erg. We get numerical optical lightcurves in good agreement with the observed data.

4.2 The external forward and reverse shock afterglow emission

In our modeling, it turns out that the shallow-declining part of the optical flare is hard to be accounted for (see Fig. S6). A possibility is the emergence of the reverse shock, as observed in for instance GRB 990123 (3, 5). Indeed, a reverse and forward shock scenario can reasonably reproduce the optical and X-ray data. The magnetic field in the reverse shock region should be stronger than that in the forward shock region by a factor of quite a few $\times 10$ otherwise the induced optical flash can not be brighter than the forward shock peak optical emission by a factor of ~ 1000 (7, 8). The following physical parameters are found to be able to reasonably reproduce the afterglow data: the isotropic energy is $E_{\text{iso}} = 1.0 \times 10^{55}$ erg with a half open jet angle $\theta_j = 0.025$, the initial Lorentz factor is $\Gamma = 800$, the fraction of forward and reverse shock energy given to the electrons is $\epsilon_e = 0.4$, the fraction of the forward (reverse) shock energy given to the magnetic field is $\epsilon_{b,fs} = 2.5 \times 10^{-5}$ ($\epsilon_{b,rs} = 0.3$), the number density of the interstellar medium is $n = 0.05$ cm $^{-3}$ and the power-law index for shock-accelerated electrons is $p = 2.26$. Such a p is well consistent with that needed in reproducing the optical to X-ray spectrum and lightcurves shown in Fig. S5 and Fig. S6, including *Swift* data analyzed in this work and Liverpool telescope data from GCN (38, 49).

5 The prospect of detecting ultra-luminous optical/ultraviolet flares at high redshifts with SVOM/VT

Optical/ultraviolet flares at high redshift will suffer from serious absorption. Following Moller & Jakobsen (50), we estimate the absorption correction to be $A_B \sim 5$ mag (the received photons are mainly caused by red leak of blue filter) and $A_R \sim 1$ mag for the sources at $z \sim 6$, based on the responses of SVOM/VT blue and red channels (i.e., B and R). For flares as luminous as GRB 080319B or GRB 220101A, if taken place at $z \sim 6$, then we would have $M_R \sim 10.5$ mag and $M_B \sim 15$ mag. With the shortest exposure of 1s, SVOM/VT has a dynamic range of 9 – 18 mag, which is sufficiently sensitive to catch the signals mentioned above. However, usually the exposure time of SVOM/VT should be 10-100 seconds, for which the R filter may get saturated but the B filter is not. We therefore conclude that SVOM/VT is a suitable equipment to detect the extremely bright optical flares of GRBs at $z \sim 6$.

Supplementary References

30. Poole, T. S. *et al.* Photometric calibration of the Swift ultraviolet/optical telescope. *Mon. Not. Roy. Astron. Soc.* **383**, 627–645 (2008). 0708.2259.
31. Maselli, A. *et al.* GRB 130427A: A Nearby Ordinary Monster. *Science* **343**, 48–51 (2014). 1311.5254.
32. Woźniak, P. R. *et al.* Gamma-Ray Burst at the Extreme: “The Naked-Eye Burst” GRB 080319B. *Astrophys. J.* **691**, 495–502 (2009). 0810.2481.
33. Markwardt, C. *et al.* The swift bat software guide. *NASA/GSFC, Greenbelt, MD* **6** (2007).
34. Evans, P. A. *et al.* An online repository of Swift/XRT light curves of γ -ray bursts. *Astron. Astrophys.* **469**, 379–385 (2007). 0704.0128.

35. Evans, P. *et al.* Methods and results of an automatic analysis of a complete sample of swift-xrt observations of grbs. *Monthly Notices of the Royal Astronomical Society* **397**, 1177–1201 (2009).
36. Goldstein, A., Cleveland, W. H. & Kocevski, D. Fermi gbm data tools: v1.1.0 (2021). URL <https://fermi.gsfc.nasa.gov/ssc/data/analysis/gbm>.
37. Ashton, G. *et al.* Bilby: a user-friendly bayesian inference library for gravitational-wave astronomy. *The Astrophysical Journal Supplement Series* **241**, 27 (2019).
38. Perley, D. A. GRB 220101A: Liverpool telescope imaging of a high-redshift afterglow. *GRB Coordinates Network* **31357**, 1 (2022).
39. Andersen, M. I. *et al.* VLT identification of the optical afterglow of the gamma-ray burst GRB 000131 at $z=4.50$. *Astron. Astrophys.* **364**, L54–L61 (2000). astro-ph/0010322.
40. Thöne, C. C. *et al.* GRB 100219A with X-shooter - abundances in a galaxy at $z=4.7$. *Mon. Not. Roy. Astron. Soc.* **428**, 3590–3606 (2013). 1206.2337.
41. Schlafly, E. F. & Finkbeiner, D. P. Measuring Reddening with Sloan Digital Sky Survey Stellar Spectra and Recalibrating SFD. *Astrophys. J.* **737**, 103 (2011). 1012.4804.
42. Planck Collaboration *et al.* Planck 2018 results. VI. Cosmological parameters. *Astron. Astrophys.* **641**, A6 (2020). 1807.06209.
43. Fan, Y. Z., Wei, D. M. & Wang, C. F. The very early afterglow powered by ultra-relativistic mildly magnetized outflows. *Astron. Astrophys.* **424**, 477–484 (2004). astro-ph/0405392.

44. Zhang, B. & Kobayashi, S. Gamma-Ray Burst Early Afterglows: Reverse Shock Emission from an Arbitrarily Magnetized Ejecta. *Astrophys. J.* **628**, 315–334 (2005). [astro-ph/0404140](#).

45. Geng, J. J., Wu, X. F., Huang, Y. F., Li, L. & Dai, Z. G. Imprints of Electron-Positron Winds on the Multiwavelength Afterglows of Gamma-ray Bursts. *Astrophys. J.* **825**, 107 (2016). [1605.01334](#).

46. Sironi, L., Keshet, U. & Lemoine, M. Relativistic Shocks: Particle Acceleration and Magnetization. *Space Sci. Rev.* **191**, 519–544 (2015). [1506.02034](#).

47. Giannios, D. & Spitkovsky, A. Signatures of a Maxwellian component in shock-accelerated electrons in GRBs. *Mon. Not. Roy. Astron. Soc.* **400**, 330–336 (2009). [0905.1970](#).

48. Geng, J.-J., Huang, Y.-F., Wu, X.-F., Zhang, B. & Zong, H.-S. Low-energy Spectra of Gamma-Ray Bursts from Cooling Electrons. *Astrophys. J. Supp.* **234**, 3 (2018). [1709.05899](#).

49. Perley, D. A. GRB 220101A: Additional Liverpool telescope photometry. *GRB Coordinates Network* **31425**, 1 (2022).

50. Møller, P. & Jakobsen, P. The Lyman continuum opacity at high redshifts - Through the Lyman forest and beyond the Lyman valley. *Astron. Astrophys.* **228**, 299–309 (1990).

51. Li, W. *et al.* The Calibration of the Swift UVOT Optical Observations: A Recipe for Photometry. *Publ. Astron. Soc. Pac.* **118**, 37–61 (2006). [astro-ph/0505504](#).

52. Kuin, N. P. M. & Rosen, S. R. The measurement errors in the Swift-UVOT and XMM-OM. *Mon. Not. Roy. Astron. Soc.* **383**, 383–386 (2008). [0709.1208](#).

Supplementary Tables

T-T ₀ (s)	Exp (s)	V (AB)	B (AB)	U (AB)	W1 (AB)	M2 (AB)	W2 (AB)
367.38	19.46	12.67±0.04
391.76	19.45	12.01±0.04
416.18	19.45	12.65±0.04	...
440.84	19.44	12.60±0.04
465.10	19.44	12.09±0.38 ^a
490.09	19.45	...	11.28±0.40 ^a
540.86	19.44	13.12±0.04
565.28	19.40	12.41±0.04
589.61	19.46	13.04±0.04	...
614.82	19.44	13.06±0.04
639.13	19.46	12.90±0.07 ^a
663.96	19.46	...	12.69±0.04
713.68	19.45	13.50±0.04
737.97	19.44	12.65±0.04
762.19	19.44	13.30±0.04	...
786.88	19.44	13.31±0.04
811.16	19.44	13.06±0.04
835.91	19.45	...	12.98±0.04
1136.89	19.45	13.50±0.04
1161.73	19.46	...	13.39±0.04
1213.17	19.44	14.10±0.04
1237.51	19.44	13.34±0.05
1261.91	19.43	13.92±0.05	...
1286.75	19.44	13.90±0.04
1311.01	19.45	13.73±0.04
1335.68	19.44	...	13.60±0.04
1385.28	19.40	14.20±0.04
1409.66	19.43	13.53±0.05
1433.98	19.45	14.09±0.05	...
1458.64	19.44	14.08±0.04
1482.87	19.44	13.82±0.04
1508.07	19.45	...	13.77±0.04
1557.68	19.44	14.39±0.04
1581.95	19.45	13.69±0.05
1606.20	19.44	14.25±0.05	...
1630.88	19.45	14.24±0.04
1655.08	19.41	13.98±0.04
1679.93	19.44	...	13.87±0.04
1729.85	19.44	14.42±0.04
1754.32	19.46	13.76±0.05
1779.91	19.55	14.28±0.05	...
1804.55	19.45	14.30±0.04
1828.75	19.45	14.08±0.04
1853.48	19.45	...	13.90±0.04
1903.00	19.44	14.52±0.05
1927.21	19.45	13.81±0.05
1951.62	19.45	14.38±0.05	...

^a. Taken from Maselli et al. (31).

Table S1: **Early observations of GRB 130427A by *Swift*-UVOT.** Galactic extinction $A_V = 0.055$, $A_B = 0.071$, $A_U = 0.087$, $A_{W1} = 0.118$, $A_{M2} = 0.163$ and $A_{W2} = 0.156$ have been applied. These data points have been plotted in the left panel of Fig. S2.

Epoch	T-T ₀ (s)	Exp (s)	V (AB)	B (AB)	U (AB)	W1 (AB)	M2 (AB)	W2 (AB)	White ^a (AB)
1	515.57	19.44	12.32±0.04	11.51±0.35 ^b	12.31±0.30 ^b	12.82±0.04	12.89±0.04	13.05±0.04	12.62±0.44
2	688.49	19.45	12.59±0.04	12.79±0.04	12.93±0.06	13.18±0.04	13.20±0.04	13.45±0.04	12.95±0.06
3	860.19	19.45	12.82±0.04	13.00±0.04	13.11±0.04	13.41±0.04	13.44±0.04	13.75±0.04	13.19±0.09
4	1187.86	19.44	13.28±0.05	13.42±0.04	13.58±0.04	13.80±0.04	13.85±0.04	14.08±0.04	13.60±0.06
5	1359.98	19.45	13.48±0.05	13.63±0.04	13.77±0.04	13.98±0.04	14.02±0.05	14.18±0.04	13.77±0.05
6	1532.32	19.44	13.65±0.05	13.78±0.04	13.86±0.04	14.15±0.04	14.19±0.05	14.37±0.04	13.93±0.05
7	1704.19	19.44	13.75±0.05	13.88±0.04	14.02±0.04	14.28±0.04	14.27±0.05	14.41±0.04	14.03±0.05
8	1877.72	19.44	13.80±0.05	13.90±0.04 ^c	14.08±0.04 ^c	14.29±0.04 ^c	14.32±0.05	14.50±0.05	14.07±0.05

a. Interpolated White band AB magnitude of GRB 130427A. To derive the intrinsic count rate in a 5 arcsec aperture, galactic extinction $A_{\text{WH}} = 0.0875$ have been accounted. Fitting uncertainties and standard deviation of fitting residuals contribute to uncertainties have been considered.

b. At early phase, there is an additional radiation component, hence these 2 data points are excluded from SED fitting algorithm.

c. These data points are results of extrapolation, hence they are excluded from SED fitting algorithm as well.

Table S2: White band emission interpolated by *Swift*-UVOT narrow bands. These data (except for the last column) have been plotted in the right panel of Fig. S2.

T-T ₀ (s)	Exposure (s)	$\dot{N}_{\text{ring}}^{\text{tot,raw}}$ (count/s)	$\dot{N}_{\text{ring}}^{\text{bkg,raw}}$ (count/s)	COI _{tot(bkg)}	LSS	\dot{N}_{ring} (count/s)	\dot{N}_{aper} (count/s)
GRB 220101A							
165.95	27.56	83.08 \pm 1.86	74.07 \pm 1.18	1.033(1.029)	0.998	11.23 \pm 2.75	257.17 \pm 22.69
209.76	58.67	79.73 \pm 1.25	73.84 \pm 0.81	1.031(1.029)	0.998	7.28 \pm 1.85	150.41 \pm 5.44
GRB 130427A ^a							
515.57	19.44	139.77 \pm 3.05	72.21 \pm 1.21	1.056(1.028)	0.997	80.66 \pm 4.00	2030.98 \pm 831.79 ^b
688.49	19.45	133.49 \pm 2.98	72.09 \pm 1.21	1.054(1.028)	0.996	73.20 \pm 3.90	1493.50 \pm 86.74
860.19	19.45	120.21 \pm 2.83	70.98 \pm 1.21	1.048(1.028)	0.996	58.19 \pm 3.69	1204.35 \pm 101.10
1187.86	19.44	102.65 \pm 2.30	71.17 \pm 1.06	1.041(1.028)	0.996	36.99 \pm 3.00	826.44 \pm 43.24
1359.98	19.45	92.88 \pm 2.19	71.45 \pm 1.06	1.037(1.028)	0.996	25.09 \pm 2.86	703.53 \pm 29.41
1532.32	19.44	96.50 \pm 2.23	71.19 \pm 1.04	1.038(1.028)	0.997	29.68 \pm 2.90	608.85 \pm 30.53
1704.19	19.44	92.26 \pm 2.18	71.03 \pm 1.05	1.037(1.028)	0.997	24.86 \pm 2.84	553.88 \pm 26.34
1877.72	19.44	89.60 \pm 2.15	71.26 \pm 1.05	1.036(1.028)	0.998	21.47 \pm 2.81	531.31 \pm 26.60
RA (J2000)	DEC (J2000)	$\dot{N}_{\text{ring}}^{\text{tot,raw}}$ (count/s)	$\dot{N}_{\text{ring}}^{\text{bkg,raw}}$ (count/s)	COI _{tot(bkg)}	LSS	\dot{N}_{ring} (count/s)	\dot{N}_{aper} (count/s)
stars in GRB 220101A field ^c .							
00:05:43.983	+31:47:20.11	80.83 \pm 0.76	74.00 \pm 0.49	1.032(1.029)	1.006	8.58 \pm 1.14	168.01 \pm 4.10
00:05:33.844	+31:42:10.45	81.85 \pm 0.75	74.00 \pm 0.48	1.032(1.029)	1.014	9.94 \pm 1.12	208.39 \pm 6.07
00:05:26.211	+31:48:43.76	83.42 \pm 1.06	73.99 \pm 0.67	1.033(1.029)	0.996	11.73 \pm 1.56	230.06 \pm 7.61

a. \dot{N}_{aper} is derived from SED.

b. This data is not fitted since U-band exposures were saturated around this exposure, hence it could be unreliable(see Fig. S2).

c. These data are measured with the first 150 second White band exposure in window timing mode.

Table S3: Photon count rates measured in aperture and halo ring methods in White band. Sensitivity correction factors are 1.175 and 1.102 for GRB 220101A field and GRB 130427A field, respectively. The factor from count rate to flux is 0.01327 mJy/(count/s) for white band. These data points have been plotted in the left panel of Fig. S3.

T-T ₀ (s)	Exp (s)	$\dot{N}_{\text{ring}}^{\text{tot,raw}}$ (count/s)	$\dot{N}_{\text{ring}}^{\text{bkg,raw}}$ (count/s)	COI _{tot(bkg)}	\dot{N}_{ring} (count/s)	Mag _{aper^a} (AB)	\dot{N}_{aper}^b (count/s)
080319B V band measurements with Woźnika et al. as reference							
180.60	9.84	74.86 \pm 1.19	15.11 \pm 0.20	1.030(1.006)	65.43 \pm 1.35	10.06 \pm 0.02	1349.02 \pm 24.85
193.52	9.84	65.04 \pm 1.39	14.95 \pm 0.20	1.026(1.006)	54.63 \pm 1.56	10.23 \pm 0.02	1152.44 \pm 21.23
206.25	9.85	54.36 \pm 1.50	14.77 \pm 0.19	1.021(1.006)	43.01 \pm 1.67	10.44 \pm 0.02	952.40 \pm 17.54
218.97	9.85	52.19 \pm 1.52	14.94 \pm 0.20	1.020(1.006)	40.43 \pm 1.68	10.55 \pm 0.02	861.43 \pm 15.87
231.70	9.84	47.80 \pm 1.53	14.35 \pm 0.19	1.019(1.006)	36.23 \pm 1.69	10.72 \pm 0.02	731.85 \pm 13.48
244.43	9.84	42.70 \pm 1.53	14.32 \pm 0.19	1.017(1.006)	30.68 \pm 1.68	10.88 \pm 0.02	635.65 \pm 11.71
257.45	9.84	39.72 \pm 1.52	14.38 \pm 0.19	1.015(1.006)	27.36 \pm 1.67	11.00 \pm 0.02	567.05 \pm 10.45
270.38	9.84	38.63 \pm 1.51	14.77 \pm 0.19	1.015(1.006)	25.75 \pm 1.66	11.12 \pm 0.02	509.59 \pm 9.39
283.30	9.84	36.73 \pm 1.50	14.34 \pm 0.19	1.014(1.006)	24.15 \pm 1.64	11.23 \pm 0.02	457.95 \pm 8.44
296.23	9.84	35.39 \pm 1.49	14.10 \pm 0.19	1.014(1.005)	22.94 \pm 1.63	11.36 \pm 0.02	408.53 \pm 7.53
309.15	9.84	31.18 \pm 1.45	14.37 \pm 0.19	1.012(1.006)	18.09 \pm 1.58	11.52 \pm 0.02	351.58 \pm 6.48
322.08	9.84	28.19 \pm 1.41	14.05 \pm 0.19	1.011(1.005)	15.20 \pm 1.54	11.61 \pm 0.02	323.91 \pm 5.97
334.80	9.84	28.53 \pm 1.41	14.00 \pm 0.19	1.011(1.005)	15.62 \pm 1.54	11.72 \pm 0.02	291.08 \pm 5.36
360.05	29.52	24.58 \pm 0.78	14.14 \pm 0.11	1.010(1.005)	11.21 \pm 0.85	11.91 \pm 0.02	244.35 \pm 4.50
395.50	29.52	23.49 \pm 0.77	13.98 \pm 0.11	1.009(1.005)	10.21 \pm 0.84	12.20 \pm 0.02	187.25 \pm 3.45
431.04	29.53	22.41 \pm 0.76	14.19 \pm 0.11	1.009(1.005)	8.82 \pm 0.82	12.40 \pm 0.02	156.18 \pm 2.88
466.29	29.52	21.29 \pm 0.74	14.14 \pm 0.11	1.008(1.005)	7.67 \pm 0.81	12.54 \pm 0.02	137.03 \pm 2.52
502.44	29.52	20.02 \pm 0.73	13.90 \pm 0.11	1.008(1.005)	6.55 \pm 0.79	12.74 \pm 0.02	137.03 \pm 2.52
537.68	29.52	19.13 \pm 0.72	13.96 \pm 0.11	1.007(1.005)	5.53 \pm 0.78	12.80 \pm 0.02	114.29 \pm 2.11
080319B V band measurements with Page et al. as reference							
189.92	29.49	67.15 \pm 0.79	14.97 \pm 0.11	1.026(1.006)	56.97 \pm 0.88	10.07 \pm 0.26	1335.42 \pm 319.79
224.89	39.36	49.06 \pm 0.76	14.58 \pm 0.10	1.019(1.006)	37.38 \pm 0.84	10.44 \pm 0.29	949.77 \pm 253.68
269.89	49.21	38.26 \pm 0.67	14.48 \pm 0.09	1.015(1.006)	25.67 \pm 0.74	10.89 \pm 0.38	627.51 \pm 219.62
322.39	54.13	29.98 \pm 0.61	14.06 \pm 0.08	1.012(1.005)	17.13 \pm 0.67	11.60 \pm 0.74	326.30 \pm 222.40
080319B V band measurements with HEASoft							
322.39	54.13	29.98 \pm 0.61	14.06 \pm 0.08	1.012(1.005)	17.13 \pm 0.67	11.75 \pm 0.02	284.20 \pm 5.24 ^c
357.39	14.77	23.47 \pm 1.09	14.15 \pm 0.16	1.009(1.005)	10.00 \pm 1.18	11.91 \pm 0.04	245.26 \pm 9.04
372.39	14.76	24.23 \pm 1.10	14.37 \pm 0.16	1.009(1.006)	10.58 \pm 1.20	12.10 \pm 0.04	205.88 \pm 7.58
387.39	14.77	24.79 \pm 1.11	14.16 \pm 0.16	1.010(1.005)	11.40 \pm 1.21	12.14 \pm 0.04	198.44 \pm 7.31
402.40	14.77	22.70 \pm 1.08	13.84 \pm 0.15	1.009(1.005)	9.51 \pm 1.17	12.21 \pm 0.04	186.05 \pm 6.85
417.40	14.76	22.44 \pm 1.07	14.46 \pm 0.16	1.009(1.006)	8.56 \pm 1.17	12.35 \pm 0.04	163.54 \pm 6.02
432.40	14.77	22.51 \pm 1.07	14.14 \pm 0.16	1.009(1.005)	8.97 \pm 1.17	12.44 \pm 0.04	150.53 \pm 5.55
447.40	14.76	20.96 \pm 1.05	13.89 \pm 0.15	1.008(1.005)	7.58 \pm 1.14	12.49 \pm 0.04	143.75 \pm 5.30
462.40	14.77	21.64 \pm 1.06	14.21 \pm 0.16	1.008(1.005)	7.96 \pm 1.15	12.51 \pm 0.04	141.13 \pm 5.20
477.40	14.76	21.09 \pm 1.05	14.22 \pm 0.16	1.008(1.005)	7.36 \pm 1.14	12.60 \pm 0.04	129.90 \pm 4.79
492.39	14.77	21.44 \pm 1.06	13.95 \pm 0.15	1.008(1.005)	8.03 \pm 1.15	12.62 \pm 0.04	127.53 \pm 4.70
507.39	14.76	19.91 \pm 1.03	13.98 \pm 0.15	1.008(1.005)	6.35 \pm 1.12	12.77 \pm 0.04	111.08 \pm 4.09
522.39	14.77	19.06 \pm 1.01	13.82 \pm 0.15	1.007(1.005)	5.60 \pm 1.10	12.79 \pm 0.04	109.05 \pm 4.02
537.40	14.77	19.94 \pm 1.03	13.76 \pm 0.15	1.008(1.005)	6.62 \pm 1.12	12.88 \pm 0.04	100.37 \pm 3.70
552.40	14.76	19.08 \pm 1.01	14.00 \pm 0.16	1.007(1.005)	5.43 \pm 1.10	12.89 \pm 0.04	99.45 \pm 3.66
567.30	14.57	18.62 \pm 1.01	14.19 \pm 0.16	1.007(1.005)	4.75 \pm 1.10	12.94 \pm 0.04	94.98 \pm 3.50 ^d
719.60	19.47	16.60 \pm 0.84	13.88 \pm 0.13	1.006(1.005)	2.90 \pm 0.91	13.35 \pm 0.04	65.11 \pm 2.40 ^d
1073.88	196.67	15.55 \pm 0.26	14.04 \pm 0.04	1.006(1.005)	1.61 \pm 0.28	14.13 \pm 0.02	31.74 \pm 0.58 ^d
1273.77	196.77	15.34 \pm 0.25	14.16 \pm 0.04	1.006(1.005)	1.26 \pm 0.28	14.52 \pm 0.02	22.16 \pm 0.41 ^d

a. Magnitudes are taken from Woźnika et al. (32) and Page et al. (20). It is not necessary to take account for the very small(~ 0.01) difference between Vega magnitude and AB magnitude in V band.

b. Only values in the last sub table 080319B V band measurements with HEASoft are directly measured, others are all inferred values(i.e. \dot{N}_{int}).

c. This exposure is close to saturation, and Page et al. (20) derived a photometry result with readout streak method, which is consistent with the aperture photometry result given by HEASoft.

d. These points are not plotted in Fig 3 and not used in fitting algorithm as well.

Table S4: Photon count rates measured in aperture and halo ring methods in v band. The large scale structure correction factor and the sensitivity correction factor are 1.001 and 1.056, respectively. The factor from count rate to flux is 0.25491 mJy/(count/s) for V band. These data points used have been plotted in the right panel of Fig. 3.

Filter	T _{start} second	T _{end} second	T _{exp} second	Signal ^a count/s	Sky count/s/pixel	Mag ^b (AB)
v	70.94	80.61	9.52	6.137 ± 1.074	0.0313	16.12 ± 0.19
white	91.96	93.62	1.64	21.74 ± 4.74	0.0145	17.75 ± 0.24
white	93.64	97.62	3.93	50.37 ± 4.79	0.0148	16.83 ± 0.10
white	97.63	101.62	3.94	123.7 ± 8.9	0.0150	15.86 ± 0.08
white	101.63	105.63	3.94	360.4 ± 30.3	0.0147	14.70 ± 0.09
white	105.64	109.62	3.93	(634.4 ± 171.8) ^c	0.0146	(14.08 ± 0.29)
white	109.63	113.63	3.94	(765.0 ± 175.6) ^c	0.0147	(13.88 ± 0.25)
white	113.64	117.62	3.93	(1033 ± 184.4) ^c	0.0150	(13.56 ± 0.19)
white	117.63	121.63	3.94	(544.8 ± 168.7) ^c	0.0146	(14.25 ± 0.34)
white	121.64	125.62	3.93	(570.2 ± 170.7) ^c	0.0147	(14.20 ± 0.33)
white	125.63	129.62	3.94	(374.0 ± 165.0) ^c	0.0148	(14.66 ± 0.48)
white	129.64	133.62	3.93	(411.7 ± 167.3) ^c	0.0149	(14.55 ± 0.44)
white	133.63	137.62	3.94	(383.1 ± 165.9) ^c	0.0149	(14.63 ± 0.47)
white	137.63	141.62	3.93	(333.5 ± 163.1) ^c	0.0146	(14.78 ± 0.53)
white	141.63	145.62	3.94	(381.1 ± 163.3) ^c	0.0145	(14.64 ± 0.47)
white	145.63	149.63	3.94	(346.4 ± 163.6) ^c	0.0147	(14.74 ± 0.51)
white	149.64	153.62	3.93	330.2 ± 26.4	0.0148	14.79 ± 0.09
white	153.63	157.63	3.94	328.3 ± 26.1	0.0147	14.80 ± 0.09
white	157.64	161.62	3.93	303.1 ± 23.3	0.0149	14.89 ± 0.08
white	161.63	165.63	3.94	291.6 ± 22.0	0.0145	14.93 ± 0.08
white	165.64	169.62	3.93	257.8 ± 18.7	0.0147	15.06 ± 0.08
white	169.63	173.62	3.94	224.0 ± 15.8	0.0149	15.21 ± 0.08
white	173.63	177.62	3.93	215.8 ± 15.2	0.0146	15.26 ± 0.08
white	177.63	181.62	3.94	202.9 ± 14.2	0.0148	15.32 ± 0.08
white	181.63	185.62	3.93	208.6 ± 14.6	0.0149	15.29 ± 0.08
white	185.63	189.62	3.94	186.0 ± 12.9	0.0147	15.42 ± 0.08
white	189.63	193.63	3.94	192.9 ± 13.4	0.0146	15.38 ± 0.08
white	193.64	197.62	3.93	179.6 ± 12.5	0.0147	15.45 ± 0.08
white	197.63	201.62	3.94	164.6 ± 11.5	0.0147	15.55 ± 0.08
white	201.64	205.62	3.93	187.3 ± 13.1	0.0149	15.41 ± 0.08
white	205.63	209.62	3.94	146.1 ± 10.3	0.0145	15.68 ± 0.08
white	209.64	213.62	3.93	158.1 ± 11.1	0.0148	15.59 ± 0.08
white	213.63	217.62	3.94	147.3 ± 10.4	0.0149	15.67 ± 0.08
white	217.63	221.63	3.94	134.1 ± 9.6	0.0149	15.77 ± 0.08
white	221.64	225.62	3.93	135.8 ± 9.7	0.0147	15.76 ± 0.08
white	225.63	229.63	3.94	117.3 ± 8.5	0.0145	15.92 ± 0.08
white	229.64	233.62	3.93	118.3 ± 8.6	0.0146	15.91 ± 0.08
white	233.63	237.63	3.94	114.9 ± 8.4	0.0143	15.94 ± 0.08
white	237.64	239.56	1.90	102.2 ± 10.9	0.0145	16.07 ± 0.12
<hr/>						
H/L ^d						
u	3627.5	3827.3	196.6	0.0194 ± 0.1266	0.0384	> 20.74
b	3832.6	4032.4	196.6	0.1181 ± 0.1624	0.0635	> 19.95
white	4037.3	4237.1	196.6	0.4286 ± 0.1266	0.1187	21.90 ± 0.32
w2	4242.9	4442.6	196.6	-0.3402 ± 0.0613	0.0012	> 21.54
v	4447.6	4647.4	196.6	0.4469 ± 0.0617	0.0151	18.66 ± 0.15
m2	4652.4	4852.1	196.6	0.0015 ± 0.0168	0.0006	> 21.25
w1	4857.5	5057.3	196.6	0.0099 ± 0.0308	0.0019	> 21.33
u	5062.2	5201.4	137.0	0.0659 ± 0.0730	0.0080	> 20.90
white	10266	11051	765	0.3408 ± 0.0502	0.0602	22.15 ± 0.16
v	21543	22361	798	0.1786 ± 0.0280	0.0141	19.66 ± 0.17
white	27727	28549	802	0.1635 ± 0.0396	0.0594	22.95 ± 0.26
v	39724	40112	378	0.1419 ± 0.0340	0.0138	19.91 ± 0.26
white	44845	46039	1137	0.1662 ± 0.0492	0.0601	22.93 ± 0.36
white	50868	61521	1528	0.1369 ± 0.0530	0.1073	23.13 ± 0.42
white	66833	85013	5485	0.0202 ± 0.0378	0.1000	> 23.33

a. Signal photon count rates have been corrected for coincidence losses (30, 51) and long-term sensitivity correction.

b. Magnitudes are based on *Swift*/UVOT zeropoints (30), errors are adjusted by a binomial distribution (52), limiting magnitudes are 3σ upper limits. These values have not been corrected for the Galactic extinctions of $E(B - V) = 0.0483$ (41).

c. These data have been analyzed in ring apertures as introduced in supplementary materials.

d. Images taken before are in high resolution, our photometry is in 5'' aperture, after are in low resolution, our photometry is in 3'' aperture.

Table S5: Photometry for *Swift* UVOT observations of GRB 220101A.

GRB	z	Band	M_{peak} AB	$A_{V,\text{MW}}$	β $f_{\nu} \propto \nu^{-\beta}$	A_{λ}^a	DM^c	M_{abs} AB	Ref.
990123	1.600	White to V	$M_V = 8.86 \pm 0.02$	0.04	0.67	0.04	45.42	-36.60	(3)
050904	6.295	White to 9500Å	$M = 12.13 \pm 0.24^b$	0.16	1.0	1.25	48.97	-38.09	(23)
080319B	0.937	White to V	$M_V = 5.34 \pm 0.04$	0.03	0.5	0.03	43.99	-38.68	(9)
220101A	4.618	White to V	$M_{\text{wh}} = 13.56 \pm 0.19$	0.15	0.7	4.78	48.19	-39.41	This work

a. $A_{\lambda} = A_{\lambda,\text{MW}} + A_{\lambda,\text{host}} + A_{\lambda,\text{IGM}}$ is derived from photometric SED fit.

b. Converted from $f_{\lambda=9500\text{\AA}} = 17 \pm 4 \times 10^{-15} \text{ erg cm}^{-2} \text{ s}^{-1} \text{ \AA}^{-1}$.

c. Absolute Magnitude at the peak $M_{\text{peak,abs}} = M_{\text{peak}} - DM - A_{\lambda}$.

Table S6: **Properties of extremely bright GRB flares at the peak.**

Supplementary Figures

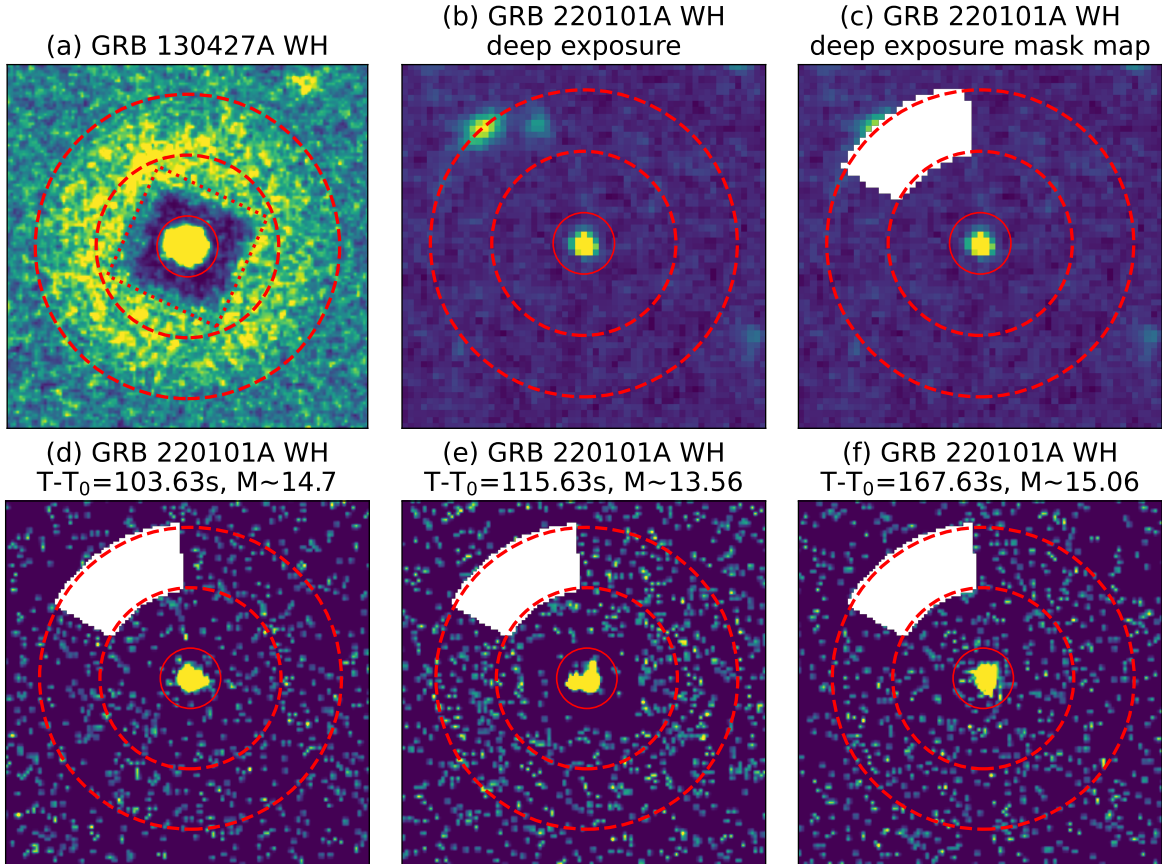


Figure S1: *Swift/UVOT white (WH) band images demonstrating the halo ring photometry method.* Panel (a) is the White band image of GRB 130427A, where the solid circle represents the standard aperture of UVOT with a radius of 5 arcsec. The dotted square region strongly suffered from coincidence loss with a typical side length of ~ 20 arcsec. Dashed annulus with an inner radius of 15 arcsec and an out radius of 25 arcsec is the halo ring region defined in this work, for which the N_{ring} is derived. Panel (b) shows the deep exposure of GRB 220101A field in White band, which reveals 2 faint sources in the halo ring region, hence we masked the annulus region from 95° to 150° , as shown in panel (c). In addition, images of panel (b) and (c) have a pixel scale of 1.004 arcsec/pixel instead of 0.502 arcsec/pixel for other 4 images. Panel (d), (e) and (f) show some images around the peak time of GRB 220101A. We measured count rates in unmasked annulus region and corrected it to the whole annulus region.

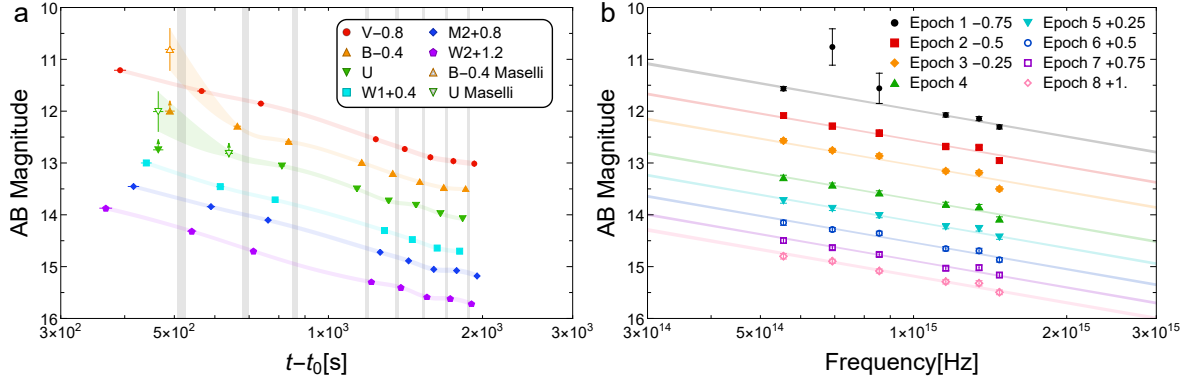


Figure S2: The UVOT lightcurves (left) as well as the SEDs (right) of GRB 130427A. In the left panel, the vertical grey regions mark the observation periods of the White filter. Note that the second U-band data is saturated, which was however a detection point in Maselli et al. (31) if only event data in the last 6s was measured, hence the filled and the empty green triangles coincide. The shaded colorful regions across photometry points are our interpolation results of light curve. The right panel presents the optical to ultraviolet SEDs at the White band observation times constructed with the extrapolated UVOT narrow band data. A single power-law spectrum well reproduces the data, as anticipated in the fireball external forward shock afterglow model, with which a reliable evaluation of the White band emission is yielded, as reported in the last column of Table S2.

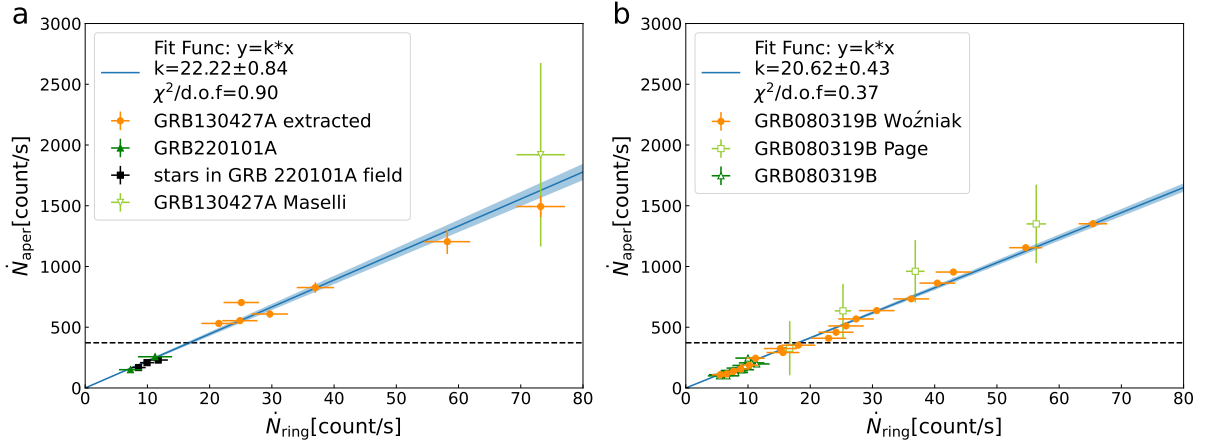


Figure S3: Photon count rates in 5'' aperture \dot{N}_{aper} (directly measured or inferred from the intrinsic value \dot{N}_{int}) and 15 – 25'' ring \dot{N}_{ring} (coincidence loss corrected) for some *Swift*/UVOT white and V band measurements. The left panel is for the White band. The dark green upward triangles represent the two unsaturated measurements of GRB 220101A in the tail phase of the flash. The filled squares are for three bright stars in the field of GRB 220101A. The light green downward empty triangle represents inferred \dot{N}_{aper} with the photometry result of GRB 130427A derived with readout streak method (31). As for orange points, the vertical coordinate represents the White-band emission of GRB 130427A inferred from measurements in other UVOT bands (see Fig. S2), while the horizontal coordinate is the \dot{N}_{ring} (see Fig. S1 for definition). Black squares are 3 unsaturated stars in GRB 220101A field. The right panel is for the V band. Empty dark green triangles are unsaturated measurements of GRB 080319B with *HEASoft* and empty light green squares are photometry results of GRB 080319B derived with the readout streak method (20). As for orange points, the vertical coordinate represents the photometry result of GRB 080319B observed with RAPTOR-T (32) when the UVOT observations were ongoing, while the horizontal axis represents \dot{N}_{ring} in the corresponding UVOT V-band image. The linear fit is just for filled points in both panels, and the correlation coefficients of filled points are 0.990 and 0.998 for the left and right panel, respectively. Black dashed lines represent the saturation count rate (coincidence loss corrected, $\sim 372 \text{ count s}^{-1}$) of UVOT.

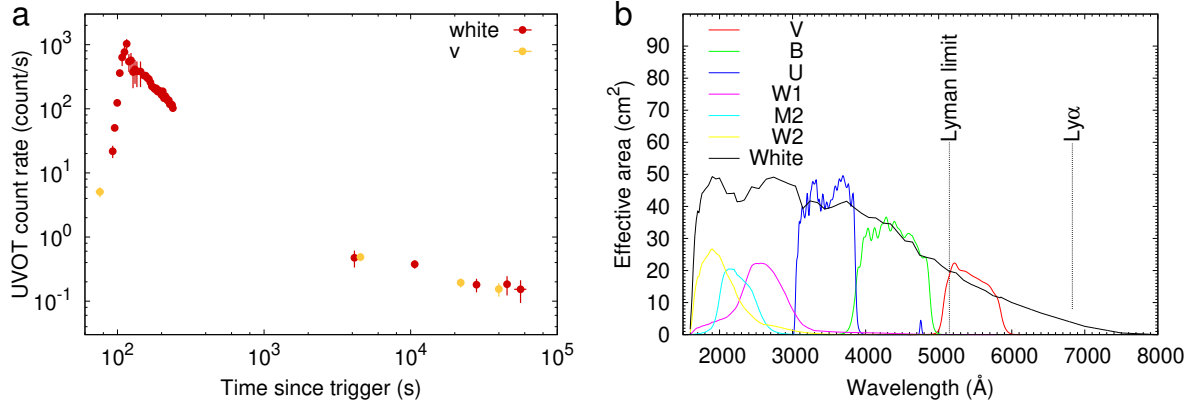


Figure S4: The similarity of *Swift*/UVOT White and V band observations of GRB 220101A. The left panel shows that the photon count rates in White band are almost the same as that in V band. This is because the photons with wavelengths below the Lyman limit (in the observer frame, it is 5124 \AA ; see the right panel) are almost fully absorbed, and the photons near the Lyman α may also suffer from strong absorption (see Fig. S5 for this effect). Therefore the collected photons are mainly within the V band.

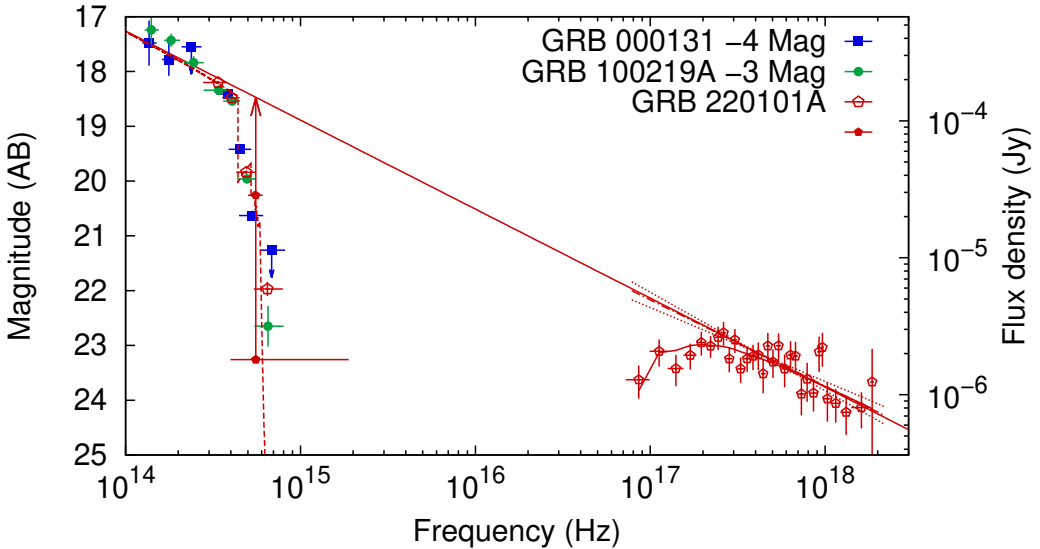


Figure S5: **Optical to X-ray SED of GRB 220101A.** *Swift* XRT, UVOT and g , r , i , z observations of Liverpool telescope in the time interval of $t \sim 0.62 - 0.68$ day after the burst (38). Such a set of ground-based telescope observation data are chosen because they are almost simultaneous with one UVOT White exposure. Neither the X-ray nor the optical emission displays a flare. Therefore, we construct the optical SED with the data collected at $t \sim 0.625$ day. We find that the absorption correction is $A_{\text{Wh}} = 4.78$ mag for intrinsic optical to X-ray spectrum with index $\beta_{\text{ox}} = 0.65$, it is well consistent with X-ray spectrum $\beta_{\text{x}} = 0.63 \pm 0.09$. The central frequency of the White band observation has been taken as the same as that of the V band because of the serious absorption of the bluer photons, as demonstrated in Fig. S4. The optical SEDs of other two GRBs 000131 (39) and 100219A (40) at similar redshifts ($z = 4.500$ and 4.667 , respectively) are also shown for comparison.

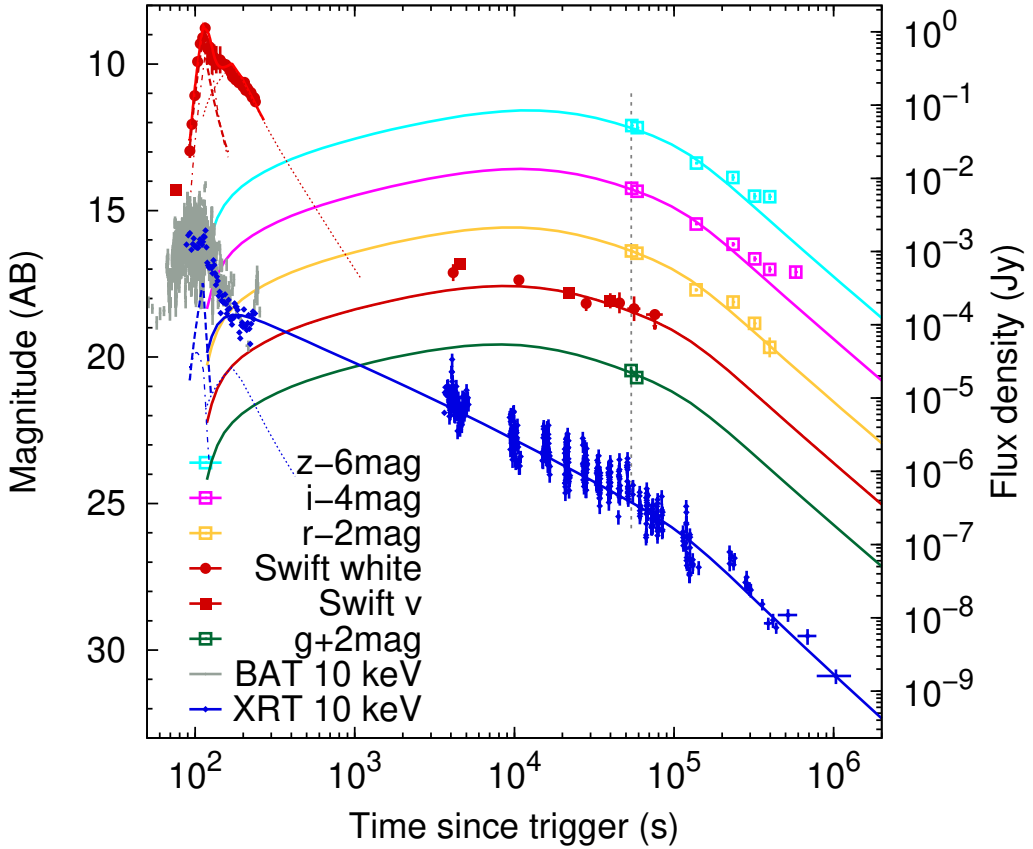


Figure S6: Fit to the multi-band afterglow lightcurves of GRB 220101A. The *Swift* XRT and UVOT data are analyzed in this work, and the other optical data are adopted from Liverpool telescope (38, 49). The total extinction corrections, including Galactic extinction and interstellar-medium extinction are $A_{\text{Wh}} = 4.78$, $A_v = 1.88$, $A_g = 3.51$, $A_r = 1.46$, $A_i = 0.24$ and $A_z = 0.10$, respectively. The dashed and dash-dotted lines represents forward and reverse shock emission arising from the weak/slow and main/fast outflow collision. Solid and dotted lines are the regular external forward and reverse shock emission of the outflow. In our calculation, the main/fast outflow was launched 92 seconds after the BAT trigger. Note that the X-ray emission at $t \leq 170$ sec was attributed to the low energy part of the prompt emission and has not been addressed in our modeling.

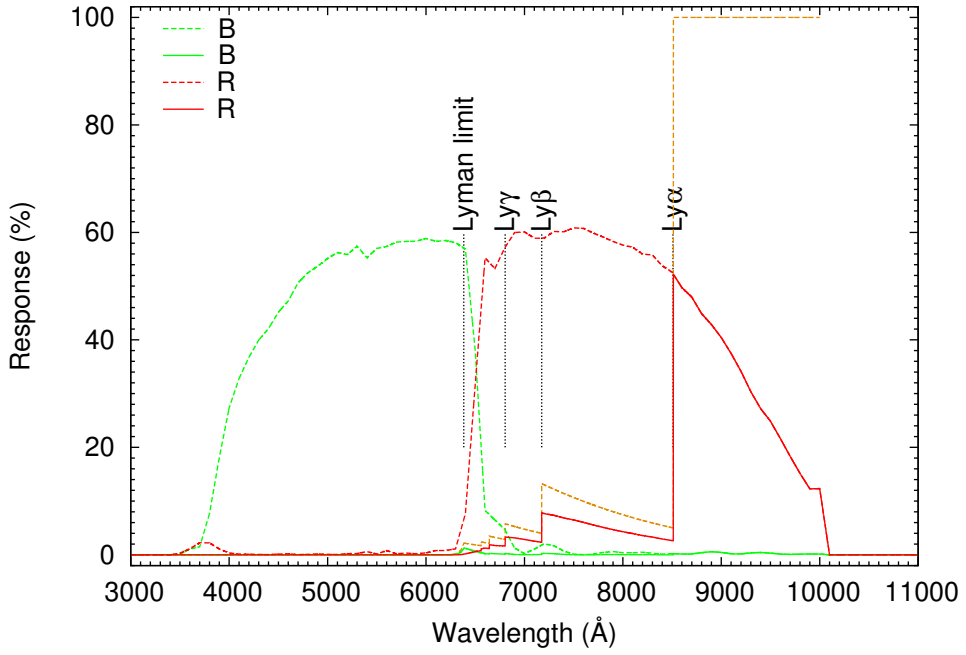


Figure S7: The response of the SVOM/VT and the Lyman absorption of the high redshift (~ 6) event. The optical/ultraviolet flash will suffer from strong absorption by intergalactic medium. Following Moller & Jakobsen (50), we find that $A_B \sim 5$ mag (the received photons are mainly caused by red leak of blue filter) and $A_R \sim 1$ mag for a source at $z = 6$, based on the responses of SVOM/VT blue and red channels (i.e., B and R). If the initial flash is as bright as that detected in GRB 080319B and GRB 220101A, the absorbed one would still be caught by SVOM/VT with a dynamic range of 9 – 18 mag for the shortest exposure of 1s. Therefore SVOM/VT is a suitable equipment to detect extremely bright optical flares of GRBs at $z \sim 6$.